

Anomalous Hall effect in thin films of the topological semimetal Co_2MnGa

Anastasios Markou,^{1,*} Dominik Kriegner,¹ Jacob Gayles,¹ Liguang Zhang,¹ Yi-Cheng Chen,¹ Benedikt Ernst,¹ Yu-Hong Lai,² Walter Schnelle,¹ Ying-Hao Chu,² Yan Sun,¹ and Claudia Felser¹

¹Max Planck Institute for Chemical Physics of Solids, Nöthnitzer Str. 40, 01187 Dresden, Germany

²Department of Materials Science and Engineering,
National Chiao Tung University, Hsinchu 30010, Taiwan

(Dated: April 7, 2022)

Topological magnetic semimetals promise large Berry curvature through the distribution of the topological Weyl nodes or nodal lines and further novel physics with exotic transport phenomena. We present a systematic study of the structural and magnetotransport properties of Co_2MnGa films from thin (20 nm) to bulk like behavior (80 nm), in order to understand the underlying mechanisms and the role on the topology. The magnetron sputtered Co_2MnGa films are $L2_1$ -ordered showing very good heteroepitaxy and a strain-induced tetragonal distortion. The anomalous Hall conductivity was found to be maximum at a value of 1138 S/cm, with a corresponding anomalous Hall angle of 13%, which is comparatively larger than topologically trivial metals. There is a good agreement between the theoretical calculations and the Hall conductivity observed for the 80 nm film, which suggest that the effect is intrinsic. Thus, the Co_2MnGa compound manifests as a promising material towards topologically-driven spintronic applications.

I. INTRODUCTION

The experimental realization of graphene, characterized by a low energy Dirac dispersion,¹ reinvigorated the interest in utilizing and understanding the topological electronic nature of materials. One such avenue led to the topological insulators determined by the surface Dirac dispersion states and gapped states in the bulk.² Contrary to topological insulators, the exotic topological semimetals are advantageous due to an intimate correlation of the dispersion of the bulk and surface states. The Dirac,^{3,4} Weyl,^{5,6} and nodal line⁷ semimetals are the most well-known examples. The Weyl semimetal (WSM) is found in systems with a lack of inversion symmetry or time reversal symmetry, where two momentum-space distributed Weyl nodes of opposite chirality form and are linked by the so-called Fermi-arc surface bands.^{8–11} The finite Berry curvature associated with the Weyl nodes or gapped nodal line leads to exotic phenomena, such as the chiral anomaly,^{12–15} magnetooptical¹⁶ and transport responses,¹⁷ the anomalous Hall effect (AHE),^{18,19} and the Nernst effect counterparts.^{20–22} In magnetic Heusler compounds, this has become a major point of interest,¹⁷ where large values of the AHE have been associated with the momentum-space distribution of the Weyl nodes and gapped nodal lines.

Recently, Wang *et al.*²³ proposed that several Co-based full Heusler compounds realize WSMs. They focused on Co_2ZrSn compound and found that two Weyl points exist close to the Fermi energy when the magnetization is along the [110] direction. Chang *et al.*²⁴ pinpointed the topological semimetal states in the Co_2TiZ ($Z = \text{Si, Ge}$ or Sn) compounds by first-principle calculations. Kübler and Felser²⁵ suggested that the experimentally observed large AHE in Co_2MnAl films²⁶ is due to the distribution

of four Weyl points just above the Fermi edge, while they, also, predicted similar results for the Co_2MnGa compound. Further, it was found to be a nodal line and Weyl semimetal.²⁷

The bulk Co_2MnGa Heusler compound crystallizes in the cubic Cu_2MnAl -type structure with space group $Fm\bar{3}m$ (No. 225) and lattice constant $a = 5.77 \text{ \AA}$. The Co atoms occupy the Wyckoff position $8c$, whereas the Mn and Ga occupy the positions $4b$ and $4a$, respectively. It is a semimetallic ferromagnet with a large saturated magnetic moment of $M_s = 4.05 \mu_B/\text{f.u.}$, following the Slater Pauling rule,²⁸ and high Curie temperature of $T_C = 694 \text{ K}$.^{29,30} Single crystals of Co_2MnGa were found to exhibit large AHE³¹ and anomalous Nernst effect (ANE),^{22,32} which originates from the large Berry curvature distribution around Fermi energy and associated with nodal lines^{27,33} or Weyl points.²⁵ Albeit, for device applications a proper understanding of the thin film limit is required. There have been some studies on thin films of Co_2MnGa , in particular, a $\text{MgO}/\text{Co}_2\text{MnGa}/\text{Pd}$ stack with perpendicular magnetic anisotropy that shows AHE³⁴ and Co_2MnGa films with one of the largest values reported for the ANE.³⁵ To fully utilize the topological properties, one must understand the dependence of the transport properties from the bulk-like films to the thin film limit. In the thin film limit, the properties of the surface play a significant role due to the intrinsic topology rooted in the electronic structure.

In this work, we present the structural, magnetic and transport properties of high-quality Co_2MnGa films with thickness ranging from 20 to 80 nm. We performed systematic x-ray diffraction (XRD), transmission electron microscopy (TEM), magnetic and transport characterization of films heteroepitaxially grown on MgO substrates. We find that the magnetotransport properties vary with the temperature and the film thickness. A strong AHE is observed in the 80 nm thick film that agrees with bulk first-principle calculations of the intrinsic AHE. Lastly, the 80 nm film shows to be the upper limit for both the

* Anastasios.Markou@cpfs.mpg.de

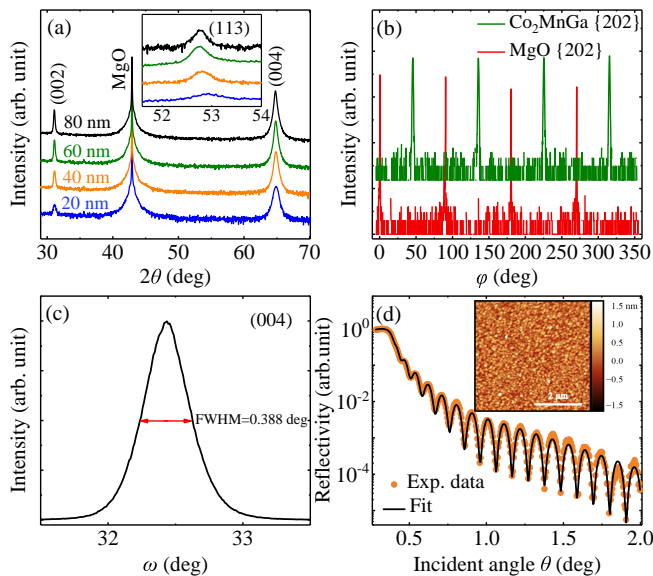


Figure 1. (a) XRD pattern of the Co_2MnGa films with different thickness (20-80 nm). The inset shows the (113) asymmetric reflections. (b) φ -scan patterns of the {202} planes from the 60 nm Co_2MnGa film and the MgO substrate. (c) Rocking curve (ω -scan) of (004) reflection from a 80 nm Co_2MnGa . (d) X-ray reflectivity pattern of the 40 nm Co_2MnGa , where the solid line represents the the least-squares fit to the data.

AHE (1138 S/cm) and anomalous Hall angle (AHA) of 13%, while the 20 nm film displays an AHE of 840 S/cm and an AHA of 10%.

II. EXPERIMENTAL DETAILS

Co_2MnGa films with thicknesses of 20, 40, 60 and 80 nm have been grown heteroepitaxially on MgO (001) single crystal substrates. A BESTEC UHV magnetron sputtering system was used for the deposition of the films, with Co (2"), Mn (2") and $\text{Mn}_{50}\text{Ga}_{50}$ (2") sources in confocal geometry. The target to substrate distance was 8". Prior to deposition, the chamber was evacuated to a base pressure less than 8×10^{-9} mbar, while the process gas (Ar 5 N) pressure was 3×10^{-3} mbar. The Co_2MnGa films were grown by co-sputtering and the individual sputter rates were adjusted to obtain the desired composition. The Co was deposited by applying 34 W dc power, the Mn by applying 6 W dc power and the $\text{Mn}_{50}\text{Ga}_{50}$ by applying 22 W dc, and the total rate was 0.58 Å/s. The substrates were rotated during deposition, to ensure homogeneous growth. The films were grown at 550 °C and then post-annealed *in situ* for an additional 20 minutes to improve the chemical ordering. All samples were capped with a 3 nm thick Al film at room temperature to prevent oxidation.

Stoichiometry was estimated as $\text{Co}_{51}\text{Mn}_{25}\text{Ga}_{24}$ by energy-dispersive x-ray spectroscopy (EDXS) with an experimental uncertainty of 2%. X-ray diffraction (XRD) and x-ray reflectivity (XRR) were measured with a Pana-

TABLE I. Lattice parameters, volume, tetragonality c/a and the full width at half maximum (FWHM) of the (004) rocking curve profile for Co_2MnGa thin films with different thickness.

Thickness (nm)	c (Å)	a (Å)	Volume (Å ³)	c/a	FWHM (deg)
20	5.728	5.811	193.4	0.986	0.495
40	5.741	5.793	192.7	0.991	0.485
60	5.751	5.785	192.4	0.994	0.424
80	5.747	5.786	192.4	0.993	0.388

lytical X'Pert³ MRD diffractometer, using $\text{CuK}\alpha_1$ radiation ($\lambda = 1.5406$ Å). The growth rates and the film thicknesses were determined by a quartz crystal microbalance and confirmed by using XRR measurements. The atomic force microscopy (AFM) image was obtained with a MFP-3D Origin⁺ microscope from Oxford Instruments Asylum Research. High-resolution scanning transmission electron microscopy (HRSTEM) was performed using a JEOL ARM200F microscope operated at 200 kV. Additionally, the JEOL was equipped with EDXS for element mapping with high spatial resolution. Diffraction patterns were collected by a FEI Tecnai operated at 200 kV. Cross-section samples were prepared by focused ion beam milling (FIB). A protective C-Pt layer was deposited on the stack before starting the cross-section preparation. Magnetization measurements were carried out using a Quantum Design (MPMS3 SQUID-VSM) magnetometer and the transport measurements were carried out on bars with a rectangular shape (7 mm x 2 mm) in a six-probe method using bonded Al wires contacts with low-frequency alternating current (ETO, PPMS9 Quantum Design).

III. RESULTS AND DISCUSSION

A. Structural properties

Different x-ray scattering measurements, 2θ - ω scan, rocking curve (ω -scan) and sample azimuth (φ) scan, were performed to study the structure, the crystallinity and the heteroepitaxial relationship between the films and the substrate, respectively. The in-plane lattice mismatch between the 45° rotated MgO unit cell ($\sqrt{2}\alpha_{\text{MgO}}$) and bulk Co_2MnGa is 3.2%, which allows the heteroepitaxial growth of (001) oriented films. Fig. 1(a) shows the XRD patterns of the 20, 40, 60 and 80 nm Co_2MnGa films. In addition to the (002) reflection of the MgO substrate, all the samples exhibit exclusively the (002) and (004) reflections of the cubic Co_2MnGa , indicating (001)-oriented films.

The properties of the Heusler compounds are strongly dependent on the occupation of the crystallographic sites. To determine if the films are fully chemically ordered in $L2_1$ -type, in addition to (002) reflection, the presence of the superstructure (111) or (113) reflections are needed.

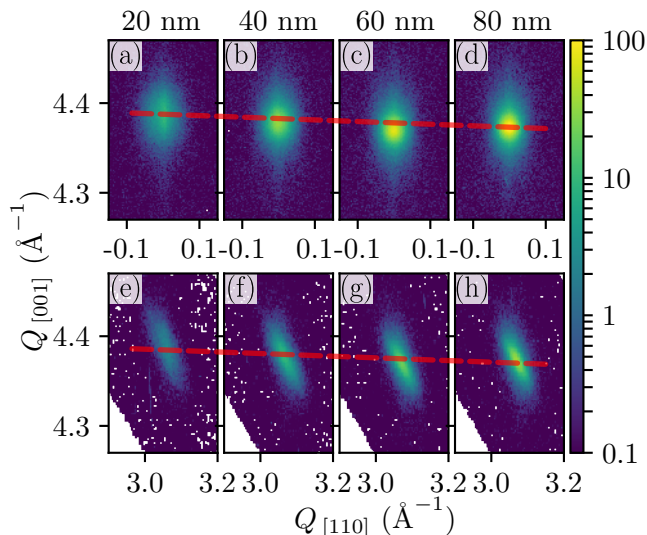


Figure 2. X-ray diffraction reciprocal space maps of Co_2MnGa thin films. Panels (a)-(e) and (f)-(j) show the diffracted intensity on a logarithmic color scale in the vicinity of the (004) and (224) Bragg peaks of the films, respectively. The x and y axis of the plot show the momentum transfer Q along the [110] and [001] directions defined as $Q_{[110]} = 4\pi/\lambda \sin\theta \sin(\omega - \theta)$, and $Q_{[001]} = 4\pi/\lambda \sin\theta \cos(\omega - \theta)$. $\lambda = 1.5406 \text{ \AA}$ is the wavelength of the x-ray radiation. Red lines are guides to the eye and show that with increasing film thickness the peak position is changing.

The inset in Fig. 1(a) shows 2θ - ω scans of the asymmetric (113) Bragg reflection of the Co_2MnGa thin films. The data were acquired in coplanar diffraction geometry with a linear detector and the acquisition software integrates along the rocking angle (ω). Quantitative analysis of the integrated intensities for all Bragg reflections, considering the diffraction geometry, as well as polarization, Lorentz, and absorption corrections³⁶ consistently showed that below 10% of $B2$ -type disorder is present in the films, which therefore can be considered almost fully chemically ordered.

φ -scan patterns of the $\{202\}$ planes from the Co_2MnGa film and the MgO substrate are depicted in Fig. 1(b). The reflections of Co_2MnGa show four-fold symmetry with 90° intervals, suggesting single crystalline epilayers with well-defined in-plane orientation. By comparing the diffractions of film and substrate a 45° in-plane rotation of the Co_2MnGa unit cell is observed with respect to the MgO substrate. The crystallographic orientation relationship is thus determined as $\text{Co}_2\text{MnGa}(001)[110] \parallel \text{MgO}(001)[100]$.

The crystal quality of the Co_2MnGa films was evaluated from the FWHM values of rocking curves measured around (004) reflection. The small FWHM $\approx 0.388^\circ$ (Fig. 1(c)) suggests that the 80 nm film shows high crystalline quality with low mosaicity. The FWHM remains below 0.5° for the thinner films indicating a very good crystal quality (Table I).

In spite of the high-temperature growth, all the films are very smooth. Fig. 1(d) shows the XRR pattern of the

40 nm Co_2MnGa film with 3 nm Al capping layer. The thickness oscillations that start after the critical angle up to 2 deg and beyond indicate smooth films and sharp interfaces. From the good agreement between the experimental data (data points) and the model curve calculated using a modified Parrat formalism³⁷ (solid line), we deduce the structural parameters, such as thickness, roughness, and density. Thickness and density agree within 2% with the nominal values and the determined substrate/film and film/capping layer roughnesses are found to be 3.4 and 4.5 \AA , respectively. The smooth surface topography is confirmed with AFM from a 40 nm thick film without Al capping layer, as depicted in the inset of Fig. 1(d). The film is continuous and very smooth with a root mean square roughness of 3 \AA , which is in good agreement with the XRR measurement.

In order to understand how the strain-induced by the substrate influences the Co_2MnGa films, we performed reciprocal space map measurements around the (004) and (224) Bragg reflections of Co_2MnGa . Fig. 2 shows that for all film thicknesses, the defined peaks are observed for both Bragg peaks, which indicates the epitaxial growth for all thicknesses. The peak position varies, which reflects a change of the lattice parameters with the film thickness. The extracted lattice parameters are summarized in Table I and show that the in-plane lattice parameter slightly decreases with thickness, while simultaneously the out-of-plane parameter increases, hence the unit cell volume remains almost constant. The thinner films display a tetragonal distortion, while thicker films approach the crystalline cubic structure found in bulk compounds. Given the reported lattice parameters of our films in Table I, we conclude that the effective symmetry of the films is reduced to space group $I4/mmm$ (No. 139).

B. TEM investigation

TEM was performed in the 80 nm thick Co_2MnGa to evaluate the film quality on the nanoscale. In Fig. 3(a) we show the cross-section HRSTEM image of the film. The high-quality growth of the Co_2MnGa film on MgO substrate is manifested by the crystal lattice of the Co_2MnGa film. Despite the lattice mismatch of 2.9% between film and substrate, the Co_2MnGa epilayer is characterized by good heteroepitaxy with no significant defects. Furthermore, the interface between film and substrate is very sharp with atomic-level flatness.

We depict the selected area electron diffraction (SAED) pattern of the same sample in Fig. 3(b), where the electron beam is parallel to the [110] zone axis of the MgO substrate. The red and blue open circles correspond to the diffraction spots from the MgO substrate and the Co_2MnGa film, respectively. The two different sets of diffraction spots are aligned, confirming the heteroepitaxial growth of the epilayer on the substrate.

Fig. 3(c) shows the high-angle annular dark-field (HAADF) STEM image, where from bottom to top the

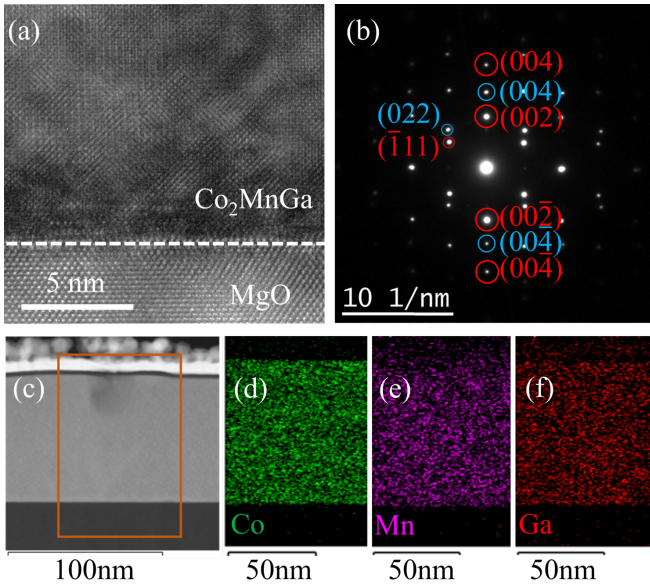


Figure 3. (a) Cross-section HRSTEM image of the 80 nm Co_2MnGa film grown on MgO substrate. (b) SAED pattern showing the diffraction spots from Co_2MnGa (blue open circles) and MgO (red open circles). (c) Cross-section HAADF-STEM image, where the orange box denotes the area, where chemical mapping was performed. Elemental mapping of (d) Co (green), (e) Mn (purple) and (f) Ga (red).

MgO substrate, the Co_2MnGa film and the Al capping layer are clearly shown in different brightness. The film is continuous, smooth and with the expected thickness of 80 nm. The element distribution within the Co_2MnGa films was analyzed by EDXS element mapping and the orange box in the HAADF-STEM image (Fig. 3(c)) indicates the area where the elemental analysis was carried out. The spatial distribution of the count rate intensity of the Co, Mn, and Ga elements are represented with different colors in Fig. 3(d)-(f). All elements were detected at exactly the same sample regions, therefore confirming the homogeneity of the Co_2MnGa .

C. Magnetic and transport properties

In Fig. 4 we show typical in-plane and out-of-plane magnetization hysteresis loops for the 80 nm Co_2MnGa film measured at 300 K. The Co_2MnGa film is a soft magnetic with an in-plane magnetic easy axis. The saturation magnetization is $M_s = 760$ kA/m and the coercivity is $\mu_0 H_c = 0.5$ mT. The Curie temperature was measured using SQUID magnetometry with an oven option. The magnetization was recorded with a constant in-plane field of $\mu_0 H = 50$ mT while warming up the sample, as shown in the inset of Fig. 4. The curve is normalized at 400 K and the extracted Curie temperature is 700 ± 5 K, which is close to the bulk value.²⁹

We show the transport properties of the Co_2MnGa films in Fig. 5. The transport measurements are collected with the magnetic field and the current applied along

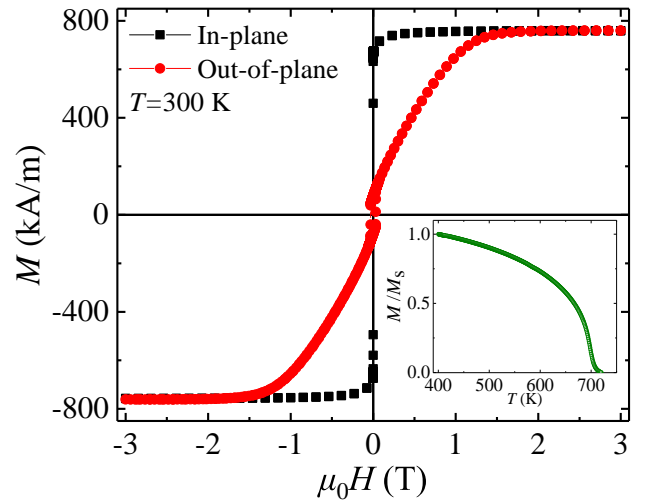


Figure 4. In-plane and out-of-plane magnetization hysteresis loops of the 80 nm Co_2MnGa film. The inset shows the temperature dependence of normalized magnetization for the 60 nm Co_2MnGa film.

the [001] and [110] directions of the Co_2MnGa , respectively. In Fig. 5(a) is depicted the temperature dependent resistivity at zero field for the 80 nm Co_2MnGa film. The film shows metallic behavior with a residual resistivity of $110 \mu\Omega \text{ cm}$ at 40 K. Above 45 K, $\rho_{xx}(T)$ is nonlinear, which indicates mixed phonon and magnon scattering state.³⁸ The upturn of longitudinal resistivity below 45 K is attributed to defects or due to diffusion channel electron-electron interaction mechanism as recently reported in $L2_1\text{-Co}_2\text{MnAl}$ films.³⁹ The inset in Fig. 5(a) shows the residual resistivity ratio ($\text{RRR} = \rho_{300\text{K}} / \rho_{40\text{K}}$) as a function of film thickness. The RRR increases linearly as the thickness increases and reaches 1.17 for the 80 nm film, which compares well with other Co-based full Heusler compound films.³⁹⁻⁴¹

In Fig. 5(b) the first quadrant of the Hall resistivity loops are shown for the 80 nm and the 20 nm at $T = 300, 75, 2$ K. We analyze the Hall resistivity in the saturated state by using

$$\rho_{yx} = R_0 \mu_0 H + \rho_{yx}^{\text{AHE}}, \quad (1)$$

where μ_0 , R_0 and $\rho_{yx}^{\text{AHE}} = R_S M$ are the permeability of free space, the ordinary Hall coefficient, R_S is the anomalous Hall coefficient and M is the magnetization perpendicular to the plane of the film, respectively. There is a clear trend that shows a saturated Hall resistivity above applied fields of 2 T for all thicknesses and temperatures. The tetragonal distortion of the Co_2MnGa films is also reflected in the Hall resistivity, where the 80 nm film, which approaches the cubic structure, saturates close to an applied field of 1.2 T and the more tetragonally distorted 20 nm film at 1.5 T. Furthermore, the magnitude of the AHE varies with the thickness and the temperature, where it is maximized at 2 K. The maximum and minimum of the Hall resistivity is found to be $\rho_{yx} = 14 \mu\Omega \text{ cm}$,

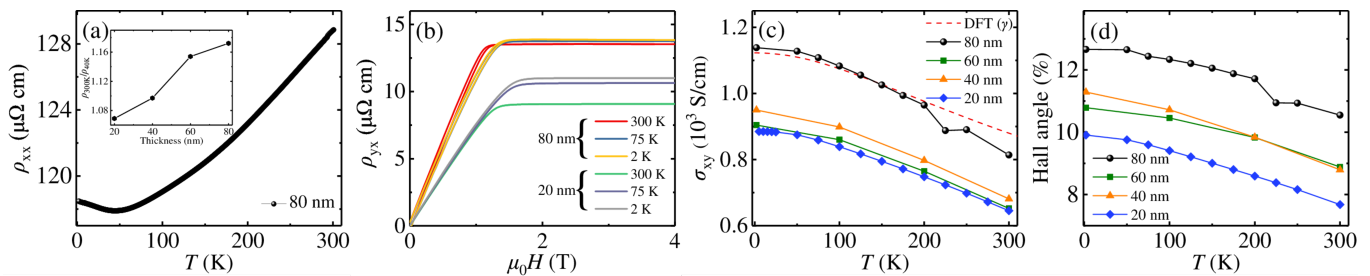


Figure 5. (a) Temperature dependent longitudinal resistivity of the 80 nm Co_2MnGa film. The inset shows the thickness dependent RRR. (b) Hall resistivity as a function of the applied magnetic field for the 80 nm and 20 nm Co_2MnGa films collected at 300, 75 and 2 K. (c) Temperature dependent Hall conductivity of Co_2MnGa films with different thickness. The red dashed line represents. (d) Temperature dependent anomalous Hall angle of Co_2MnGa films with different thickness.

and $11 \mu\Omega \text{ cm}$ for the 80 and 20 nm films, respectively. In order to compare our experimental results with theoretical calculations, we extract the Hall conductivity as a function of temperature.

The experimental values of the anomalous Hall conductivity (σ_{xy}^{AHE}) are estimated by the Hall resistivity ρ_{yx} and the longitudinal resistivity as:

$$\sigma_{xy}^{\text{AHE}} = \frac{\rho_{yx}}{\rho_{yx}^2 + \rho_{xx}^2}. \quad (2)$$

In Fig 5(c) the temperature dependence of σ_{xy}^{AHE} for all films are compared to the theoretical calculations. For all films, the largest σ_{xy}^{AHE} is observed at the lowest temperature, and is gradually reduced with increasing temperature. The thicker sample (80 nm) shows a large value of $\sigma_{xy}^{\text{AHE}} = 1138 \text{ S/cm}$ at 2 K and $\sigma_{xy}^{\text{AHE}} = 814 \text{ S/cm}$ at 300 K, which are consistent with the bulk values²², while in thinner samples the σ_{xy}^{AHE} is reduced.

We calculate the AHE in the bulk Co_2MnGa compound using interpolated tight-binding Hamiltonian on a 351^3 \mathbf{k} -grid from the first-principle electronic structure converged on a 13^3 \mathbf{k} -grid from the VASP code.⁴² The AHE is calculated using the Kubo formula within the constant γ broadening approximation:^{18,43}

$$\sigma_{ij}^{\text{AHE}} \stackrel{\gamma \rightarrow 0}{=} \frac{2e^2 \hbar}{\mathcal{N}} \sum_{\mathbf{k}, n} \sum_{m \neq n}^{\text{occ}} \text{Im} \left[\frac{\langle \psi_{\mathbf{k}, n} | v_i | \psi_{\mathbf{k}, m} \rangle \langle \psi_{\mathbf{k}, m} | v_j | \psi_{\mathbf{k}, n} \rangle}{(\mathcal{E}_{\mathbf{k}, m} - \mathcal{E}_{\mathbf{k}, n})^2 + \gamma^2} \right]. \quad (3)$$

Here, $v_i = \frac{1}{\hbar} \frac{\partial H}{\partial k_i}$ is the canonical velocity operator, and $|\psi_{\mathbf{k}, n}\rangle$ is the eigenstate of H with eigenvalue $\mathcal{E}_{\mathbf{k}, n}$. The γ dependence of the AHE in Fig. 5(c) shows an excellent agreement with the experimental results of the 80 nm film. This suggests that the 80 nm film is sufficient to reproduce the bulk properties of Co_2MnGa and that the anomalous Hall conductivity is due to the intrinsic mechanisms. The Weyl nodes and nodal lines are primarily due to the spin-up channel which leads to a suppression of spin scattering²² analogous to the case in ferromagnetic half-metals. The constant broadening does not take into account extrinsic terms such

as the side-jump and skew-scattering.⁴⁴⁻⁴⁶ Furthermore, there maybe phonon-assisted skew-scattering effects that show intrinsic behavior.⁴⁷ As the film thickness decreases the scattering introduced from the surfaces decreases the magnitude, however, the overall temperature trend does not change. $\text{MgO}/\text{Co}_2\text{MnGa}/\text{Pd}$ stacks³⁴ shows longitudinal resistivity $\sim 30 \mu\Omega \text{ cm}$ smaller and the AHE is an order of magnitude smaller ($\text{MgO}/\text{Co}_2\text{MnGa}/\text{Pd}$ stack: $\sigma_{xy}^{\text{AHE}} \approx 125 \text{ S/cm}$), compared to our films.

The anomalous Hall angle $\theta_H = \sigma_{xy}^{\text{AHE}} / \sigma_{xx}$ reflects the ability of a material to deviate the electron flow from the direction of the longitudinal electric field, due to the anomalous Hall effect. The temperature dependence of Hall angle for all Co_2MnGa films is shown in Fig. 5(d). We find that the AHA varies with the temperature and the film thickness in a similar way as the temperature dependence of the Hall conductivity. The AHA of all films has a maximum at 2-5 K and decreases with increasing temperature. A large AHA up to $\theta_H = 12.7\%$ is observed at 2 K for the 80 nm film and remains high even at room temperature ($\theta_H = 10.5\%$). The combined large values of σ_{xy}^{AHE} and θ_H in our films suggest an intrinsic mechanism with large Berry curvature in a metallic topological semimetal. The σ_{xy}^{AHE} and the θ_H of the Co_2MnGa films are similar to the $\text{Co}_3\text{Sn}_2\text{S}_2$,⁴⁸ with the gapped nodal line band structure⁴⁹. The anomalous Hall conductivity displays a similar magnitude to metallic films such as $L1_0\text{-FePt}$,⁵⁰ the noncollinear antiferromagnetic Weyl semimetals^{51,52} and the Dirac metal Fe_3Sn_2 ,⁵³ however the θ_H is an order of magnitude larger, due to the unique topological electronic structure.

IV. CONCLUSIONS

In summary, we have studied the structural and magnetotransport properties of high-quality magnetron sputtered Co_2MnGa films with varying thickness. The Co_2MnGa films are (001)-oriented and almost fully-ordered in $L2_1$ -type structure. The thinner films show a slight tetragonal distortion, whereas the thicker films approach the perfect cubic structure. Magnetic measurements reveal high magnetization and Curie temperature. The high Curie temperature of the films allows for one

to experimentally measure the large spin-splitting in the electronic structure.²⁷ The strain or composition can be tuned to shift the position of the Weyl nodes to the Fermi energy. We find that the magnetotransport properties vary with the temperature and the film thickness. The 80 nm film shows a large anomalous Hall conductivity up to 1138 S/cm, accompanied by a large anomalous Hall angle that is maximum at 13%. The strong AHE signal in the 80 nm thick film agrees very well with bulk first-principle calculations with a constant γ band broadening approximation, suggesting that the experimentally observed AHE is due to intrinsic mechanisms. Our work provides a pathway to develop thin film devices that in-

clude nodal line and Weyl topological properties intrinsic to the electronic structure.

ACKNOWLEDGMENTS

This work has been funded by the ERC Advanced Grant No. 291472 “Idea Heusler”, ERC Advanced Grant No. 742068 “TOPMAT” and EU FET Open RIA Grant No. 766566 “ASPIN”.

-
- ¹ A. H. Castro Neto, N. M. R. Peres, K. S. Novoselov, and A. K. Geim, *Rev. Mod. Phys.* **81**, 109 (2009).
- ² M. Z. Hasan and C. L. Kane, *Rev. Mod. Phys.* **82**, 3045 (2010).
- ³ S. M. Young, S. Zaheer, J. C. Y. Teo, C. L. Kane, E. J. Mele, and A. M. Rappe, *Phys. Rev. Lett.* **108**, 1 (2012).
- ⁴ Z. Wang, Y. Sun, X.-Q. Chen, C. Franchini, G. Xu, H. Weng, X. Dai, and Z. Fang, *Phys. Rev. B* **85**, 195320 (2012).
- ⁵ A. A. Burkov and L. Balents, *Phys. Rev. Lett.* **107**, 127205 (2011).
- ⁶ H. Weng, C. Fang, Z. Fang, B. Andrei Bernevig, and X. Dai, *Physical Review X* **5**, 1 (2015).
- ⁷ A. A. Burkov, M. D. Hook, and L. Balents, *Phys. Rev. B* **84**, 235126 (2011).
- ⁸ X. Wan, A. M. Turner, A. Vishwanath, and S. Y. Savrasov, *Phys. Rev. B* **83**, 205101 (2011).
- ⁹ Y. Sun, S.-C. Wu, and B. Yan, *Phys. Rev. B* **92**, 115428 (2015).
- ¹⁰ R. Batabyal, N. Morali, N. Avraham, Y. Sun, M. Schmidt, C. Felser, A. Stern, B. Yan, and H. Beidenkopf, *Sci. Adv.* **2** (2016).
- ¹¹ H. Inoue, A. Gyenis, Z. Wang, J. Li, S. W. Oh, S. Jiang, N. Ni, B. A. Bernevig, and A. Yazdani, *Science* **351**, 1184 (2016).
- ¹² D. T. Son and B. Z. Spivak, *Phys. Rev. B* **88**, 104412 (2013).
- ¹³ X. Huang, L. Zhao, Y. Long, P. Wang, D. Chen, Z. Yang, H. Liang, M. Xue, H. Weng, Z. Fang, X. Dai, and G. Chen, *Phys. Rev. X* **5**, 31023 (2015).
- ¹⁴ C.-L. Zhang, S.-Y. Xu, I. Belopolski, Z. Yuan, Z. Lin, B. Tong, G. Bian, N. Alidoust, C.-C. Lee, S.-M. Huang, T.-R. Chang, G. Chang, C.-H. Hsu, H.-T. Jeng, M. Neupane, D. S. Sanchez, H. Zheng, J. Wang, H. Lin, C. Zhang, H.-Z. Lu, S.-Q. Shen, T. Neupert, M. Zahid Hasan, and S. Jia, *Nat. Commun.* **7**, 10735 (2016).
- ¹⁵ S. A. Parameswaran, T. Grover, D. A. Abanin, D. A. Pesin, and A. Vishwanath, *Phys. Rev. X* **4**, 31035 (2014).
- ¹⁶ T. Higo, H. Man, D. B. Gopman, L. Wu, T. Koretsune, O. M. J. van 't Erve, Y. P. Kabanov, D. Rees, Y. Li, M.-T. Suzuki, S. Patankar, M. Ikhlas, C. L. Chien, R. Arita, R. D. Shull, J. Orenstein, and S. Nakatsuji, *Nat. Photonics* **12**, 73 (2018).
- ¹⁷ K. Manna, Y. Sun, L. Muechler, J. Kübler, and C. Felser, *Nat. Rev. Mater.* **3**, 244 (2018), 1802.03771.
- ¹⁸ N. Nagaosa, J. Sinova, S. Onoda, A. H. MacDonald, and N. P. Ong, *Rev. Mod. Phys.* **82**, 1539 (2010).
- ¹⁹ A. A. Burkov, *Phys. Rev. Lett.* **113**, 187202 (2014).
- ²⁰ J. Noky, J. Gooth, C. Felser, and Y. Sun, *Phys. Rev. B* **98**, 241106 (2018).
- ²¹ J. Noky, J. Gayles, C. Felser, and Y. Sun, *Phys. Rev. B* **97** (2018), 10.1103/PhysRevB.97.220405.
- ²² S. N. Guin, K. Manna, J. Noky, S. J. Watzman, C. Fu, N. Kumar, W. Schnelle, C. Shekhar, Y. Sun, J. Gooth, and C. Felser, *NPG Asia Materials* **11**, 16 (2019).
- ²³ Z. Wang, M. G. Vergniory, S. Kushwaha, M. Hirschberger, E. V. Chulkov, A. Ernst, N. P. Ong, R. J. Cava, and B. A. Bernevig, *Phys. Rev. Lett.* **117**, 236401 (2016).
- ²⁴ G. Chang, S.-Y. Xu, H. Zheng, B. Singh, C.-H. Hsu, G. Bian, N. Alidoust, I. Belopolski, D. S. Sanchez, S. Zhang, H. Lin, and M. Z. Hasan, *Sci. Rep.* **6**, 38839 (2016).
- ²⁵ J. Kübler and C. Felser, *Europhys. Lett.* **114**, 47005 (2016).
- ²⁶ E. Vilanova Vidal, G. Stryganyuk, H. Schneider, C. Felser, and G. Jakob, *Appl. Phys. Lett.* **99**, 132509 (2011).
- ²⁷ I. Belopolski, D. S. Sanchez, G. Chang, K. Manna, B. Ernst, S.-Y. Xu, S. S. Zhang, H. Zheng, J. Yin, B. Singh, G. Bian, D. Multer, X. Zhou, S.-M. Huang, B. Wang, A. Bansil, H. Lin, C. Felser, and M. Z. Hasan, (2017), arXiv:1712.09992.
- ²⁸ I. Galanakis, P. H. Dederichs, and N. Papanikolaou, *Phys. Rev. B* **66**, 174429 (2002).
- ²⁹ P. J. Webster, *J. Phys. Chem. Solids* **32**, 1221 (1971).
- ³⁰ P. J. Brown, K. U. Neumann, P. J. Webster, and K. R. A. Ziebeck, *J. Phys.: Condens. Matter* **12**, 1827 (2000).
- ³¹ K. Manna, L. Muechler, T.-H. Kao, R. Stinshoff, Y. Zhang, J. Gooth, N. Kumar, G. Kreiner, K. Koepf, R. Car, J. Kübler, G. H. Fecher, C. Shekhar, Y. Sun, and C. Felser, *Phys. Rev. X* **8**, 41045 (2018).
- ³² A. Sakai, Y. P. Mizuta, A. A. Nugroho, R. Sihombing, T. Koretsune, M.-T. Suzuki, N. Takemori, R. Ishii, D. Nishio-Hamane, R. Arita, P. Goswami, and S. Nakatsuji, *Nat. Phys.* **14**, 1119 (2018).
- ³³ G. Chang, S.-Y. Xu, X. Zhou, S.-M. Huang, B. Singh, B. Wang, I. Belopolski, J. Yin, S. Zhang, A. Bansil, H. Lin, and M. Z. Hasan, *Phys. Rev. Lett.* **119**, 156401 (2017).
- ³⁴ B. M. Ludbrook, B. J. Ruck, and S. Granville, *Appl. Phys. Lett.* **110**, 62408 (2017).
- ³⁵ H. Reichlova, R. Schlitz, S. Beckert, P. Swekis, A. Markou, Y.-C. Chen, D. Kriegner, S. Fabretti, G. Hyeon Park, A. Niemann, S. Sudheendra, A. Thomas, K. Nielsch,

- C. Felser, and S. T. B. Goennenwein, *Appl. Phys. Lett.* **113**, 212405 (2018).
- ³⁶ D. Kriegner, E. Wintersberger, and J. Stangl, *J. Appl. Cryst.* **46**, 1162 (2013).
- ³⁷ U. Pietsch, V. Hol?, and T. Baumbach, *High-Resolution X-Ray Scattering* (Springer New York, 2004).
- ³⁸ D. A. Goodings, *Phys. Rev.* **132**, 542 (1963).
- ³⁹ L. J. Zhu and J. H. Zhao, *Sci. Rep.* **7**, 42931 (2017).
- ⁴⁰ E. Vilanova Vidal, H. Schneider, and G. Jakob, *Phys. Rev. B* **83**, 174410 (2011).
- ⁴¹ M. S. Gabor, M. Belmeguenai, T. Petrisor, C. Ulhaq-Bouillet, S. Colis, and C. Tiusan, *Phys. Rev. B* **92**, 54433 (2015).
- ⁴² G. Kresse and J. Furthmüller, *Phys. Rev. B* **54**, 11169 (1996).
- ⁴³ R. Kubo, *J. Phys. Soc. Jpn.* **12**, 570 (1957).
- ⁴⁴ S. Lowitzer, D. Ködderitzsch, and H. Ebert, *Phys. Rev. Lett.* **105**, 266604 (2010).
- ⁴⁵ A. Kovalev, J. Sinova, and Y. Tserkovnyak, *Phys. Rev. Lett.* **105**, 36601 (2010).
- ⁴⁶ J. Weischenberg, F. Freimuth, J. Sinova, S. Blügel, and Y. Mokrousov, *Phys. Rev. Lett.* **107**, 106601 (2011).
- ⁴⁷ C. Gorini, U. Eckern, and R. Raimondi, *Phys. Rev. Lett.* **115**, 76602 (2015).
- ⁴⁸ E. Liu, Y. Sun, N. Kumar, L. Muechler, A. Sun, L. Jiao, S.-Y. Yang, D. Liu, A. Liang, Q. Xu, J. Kroder, V. Süß, H. Borrmann, C. Shekhar, Z. Wang, C. Xi, W. Wang, W. Schnelle, S. Wirth, Y. Chen, S. T. B. Goennenwein, and C. Felser, *Nat. Phys.* **14**, 1125 (2018).
- ⁴⁹ Q. Xu, E. Liu, W. Shi, L. Muechler, J. Gayles, C. Felser, and Y. Sun, *Phys. Rev. B* **97**, 235416 (2018).
- ⁵⁰ P. B. Allen, H. Berger, O. Chauvet, L. Forro, T. Jarlborg, A. Junod, B. Revaz, and G. Santi, *Phys. Rev. B* **53**, 4393 (1996).
- ⁵¹ S. Nakatsuji, N. Kiyohara, and T. Higo, *Nature* **527**, 212 (2015).
- ⁵² A. K. Nayak, J. E. Fischer, Y. Sun, B. Yan, J. Karel, A. C. Komarek, C. Shekhar, N. Kumar, W. Schnelle, J. Kübler, C. Felser, and S. S. P. Parkin, *Sci. Adv.* **2**, e1501870 (2016).
- ⁵³ L. Ye, M. Kang, J. Liu, F. von Cube, C. R. Wicker, T. Suzuki, C. Jozwiak, A. Bostwick, E. Rotenberg, D. C. Bell, L. Fu, R. Comin, and J. G. Checkelsky, *Nature* **555**, 638 (2018).